

Ideal and resistive edge stability calculations with M3D-C¹

Cite as: Phys. Plasmas **17**, 102508 (2010); <https://doi.org/10.1063/1.3492727>

Submitted: 02 July 2010 • Accepted: 03 September 2010 • Published Online: 21 October 2010

N. M. Ferraro, S. C. Jardin and P. B. Snyder



View Online



Export Citation

ARTICLES YOU MAY BE INTERESTED IN

[Edge localized modes and the pedestal: A model based on coupled peeling-ballooning modes](#)
Physics of Plasmas **9**, 2037 (2002); <https://doi.org/10.1063/1.1449463>

[Multi-region approach to free-boundary three-dimensional tokamak equilibria and resistive wall instabilities](#)

Physics of Plasmas **23**, 056114 (2016); <https://doi.org/10.1063/1.4948722>

[Extended full-MHD simulation of non-linear instabilities in tokamak plasmas](#)

Physics of Plasmas **27**, 102510 (2020); <https://doi.org/10.1063/5.0018208>

Physics of Plasmas
Features in Plasma Physics Webinars

Register Today!

The logo for AIP Publishing, featuring a stylized sunburst or fan shape to the left of the text "AIP Publishing".

Ideal and resistive edge stability calculations with M3D-C¹

N. M. Ferraro,^{1,2,a)} S. C. Jardin,³ and P. B. Snyder¹

¹General Atomics, P.O. Box 85608, San Diego, California 92186-5608, USA

²Oak Ridge Institute for Science and Education, Oak Ridge, Tennessee 37830-8050, USA

³Princeton Plasma Physics Laboratory, P.O. Box 451, Princeton, New Jersey 08543-0451, USA

(Received 2 July 2010; accepted 3 September 2010; published online 21 October 2010)

Growth rates of edge localized modes for various benchmark equilibria, including a diverted equilibrium, are calculated using the nonideal fluid code M3D-C¹. Growth rates calculated by M3D-C¹ in the ideal limit are found to agree with those calculated by ideal magnetohydrodynamics codes. The effects of nonuniform density and resistivity profiles are explored, as well as the sensitivity of growth rates to the position of the ideal vacuum-plasma interface. Growth rates of the diverted equilibrium are found to be particularly sensitive to moving this interface inward from the separatrix, but less sensitive to extending the plasma region beyond the separatrix. The resistivity profile within the plasma is found not to affect growth rates significantly; however, growth rates may be greatly reduced by treating the outer region as a resistive plasma instead of an ideal vacuum. Indeed, it is found that for typical scrape-off layer (SOL) temperatures, the resistive SOL model behaves more like an ideal plasma than a vacuum. © 2010 American Institute of Physics.

[doi:10.1063/1.3492727]

I. INTRODUCTION

In present tokamaks operating in high-confinement mode (H-mode), the steep pressure gradients at the edge are often observed to relax through frequent, intermittent discharges of energy, known as edge localized modes (ELMs). The physics of ELMs is a key issue for planned reactor scale tokamaks, such as ITER, both because the onset of ELMs constrains the pressure at the top of the edge barrier (or “pedestal height”), and because the ELM event can transport substantial heat and particle loads to plasma facing materials. If not controlled, ELMs in ITER are predicted to deliver energy to some plasma-facing components at levels at or above that which can be safely and sustainably handled.¹

A predictive understanding of the onset of type-I ELMs has been gained via the development of the peeling-ballooning model,² in which ELMs are triggered by instabilities driven by the large pressure gradients and bootstrap current in the edge. (A historical overview of the development of MHD models of ELMs can be found in the introduction to Ref. 3.) The calculation of peeling-ballooning modes at intermediate toroidal mode numbers ($n \sim 3-30$) (Refs. 4–6) has permitted quantitative tests of the model against observed ELM onset and pedestal constraints on several tokamaks in a wide variety of cases.⁴⁻¹⁰ In comparisons to experiment, peeling-ballooning mode stability has typically been calculated in the ideal magnetohydrodynamics (MHD) limit, in many cases in conjunction with a simple analytic model of diamagnetic stabilization, $\gamma_{\text{MHD}}^2 = \omega(\omega_* - \omega)$, where γ_{MHD} is the ideal MHD growth rate, ω is the complex frequency, and ω_* is the ion diamagnetic frequency.^{11,12} This model results in a threshold $\gamma_{\text{MHD}} > \omega_*/2$ for instability in the presence of diamagnetic effects, but does not account for spatial variation of ω_* (beyond using an average or typical

value of ω_* across the radial mode structure). Furthermore, other nonideal effects, such as those arising due to finite collisionality, have not yet been explored in detail. In order to test and improve upon the ω_* model of diamagnetic stabilization, and to gauge the importance of other nonideal effects accurately, it is necessary to appeal to models that include these effects self-consistently in general geometry. Recently, peeling-ballooning calculations have been undertaken using nonideal codes NIMROD,¹³⁻¹⁵ BOUT,^{16,17} and BOUT++.¹⁸ Here we use M3D-C¹ to explore ideal and non-ideal peeling-ballooning stability.

M3D-C¹ is an initial-value finite-element fluid code which has been used mainly for two-dimensional nonlinear two-fluid equilibrium calculations.¹⁹ Recently it has been modified to allow the calculation of three-dimensional linear stability of axisymmetric equilibria. The comprehensive physical model employed by M3D-C¹ allows the quantification of many nonideal effects on peeling-ballooning stability. Furthermore, the computational domain in M3D-C¹ extends across the separatrix, which allows both an accurate description of eigenmodes which cross the separatrix (as ELMs do), and allows treatment of the outer region (the region between the plasma and the wall) as a resistive plasma.

A primary goal of this paper is to verify the numerical methods of M3D-C¹ by reproducing the results of ideal calculations in the appropriate limit, in order to gain confidence in future nonideal calculations. In Sec. III B we present calculations of peeling-ballooning growth rates and show that, in the ideal limit, the M3D-C¹ results are in good agreement with those of ideal codes. In particular, we focus on comparison with results from ELITE,^{4,20,21} which itself has been benchmarked against a number of other codes including GATO,²² MISHKA,²³ DCON,²⁴ CASTOR,²⁵ MARG2D/MINERVA,^{26,27} BAL-MS, ILSA,²⁸ MARS,²⁹ BOUT++, and NIMROD. This comparison is carried out for three equilibria: CBM18, a circular cross-section case; DBM18, an elongated limited case; and

^{a)}Electronic mail: ferraro@fusion.gat.com.

MEUDAS1, a diverted case in JT-60U-like geometry. These equilibria are described in more detail in Sec. III A.

We then extend these results by exploring the sensitivity of the growth rates to the density and resistivity profiles in the edge and in the outer region. Due to the singularity at the active x-point of diverted plasmas, most ideal codes do not extend the ideal plasma region fully to the separatrix, but rather place the plasma-vacuum interface slightly within the separatrix. The sensitivity of peeling-ballooning growth rates to the location of this interface is calculated in Sec. III C.

II. NUMERICAL METHODS

M3D- C^1 implements a set of visco-resistive two-fluid equations similar to the Braginskii equations,³⁰ although transport coefficients are not constrained to take the Braginskii values or scalings.¹⁹ These equations may include anisotropic thermal diffusivity and viscosity, including gyroviscosity. In the present benchmark, in which we seek to obtain results in the limit of ideal MHD, the dissipative terms (except resistivity), two-fluid terms, and gyroviscosity are neglected. Although M3D- C^1 has the option of using reduced MHD models, we use the full, compressible fluid model here. For the single-fluid cases discussed here, density perturbations and momentum advection do not contribute to the linear system, and are therefore neglected. Thus, the model under consideration is

$$\rho \frac{\partial \vec{u}}{\partial t} = \vec{J} \times \vec{B} - \nabla p, \quad (1)$$

$$\frac{\partial p}{\partial t} = -\vec{u} \cdot \nabla p - \Gamma p \nabla \cdot \vec{u}, \quad (2)$$

$$\frac{\partial \vec{B}}{\partial t} = -\nabla \times \vec{E}, \quad (3)$$

where the current density and electric field are defined as

$$\vec{J} = \nabla \times \vec{B}, \quad (4)$$

$$\vec{E} = -\vec{u} \times \vec{B} + \eta \vec{J} \quad (5)$$

and \vec{u} is the fluid velocity.

The domain is discretized in the poloidal plane using triangular C^1 finite elements.³¹ The C^1 elements allow the efficient use of a flux/potential representation of the velocity and magnetic field, which results in fourth-order differential operators.³² This representation has the advantages that the magnetic field \vec{B} is manifestly divergence free, and also that it is possible to represent displacements which manifestly do not compress the toroidal magnetic field. Furthermore, the flux representation allows easy identification of magnetic surfaces in (R, Z) coordinates, which is exploited in Sec. III B to approximate an ideal plasma-vacuum interface accurately. The finite elements are arranged on a fully unstructured mesh, to allow packing of resolution in regions that require it. An example of a typical mesh used in the present study is illustrated in Fig. 1. In these linear simulations, a single toroidal Fourier mode is considered at a time.

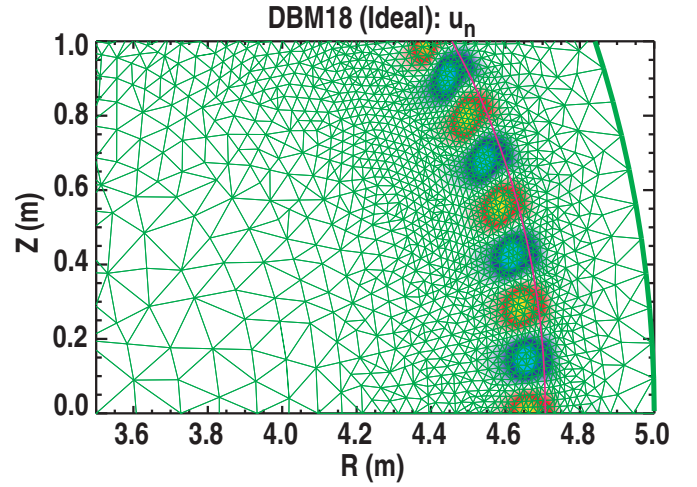


FIG. 1. (Color) A section of the $n=30$ eigenmode of the DBM18 equilibrium overlaid with the finite element mesh. The magenta line represents the foot of the pedestal.

In the split, semi-implicit time step implemented in M3D- C^1 , the velocity is advanced using a temporal discretization of the form

$$(1 - \delta t^2 \theta^2 \mathcal{L}) \vec{u}^{n+1} = (1 - \delta t^2 \alpha \mathcal{L}) \vec{u}^n + \dots, \quad (6)$$

where \mathcal{L} is the ideal MHD operator.¹⁹ Using θ -centered time differencing, one finds $\alpha = \theta(\theta - 1)$; however, it has been shown that numerical dissipation may be reduced by letting $\alpha = \theta^2$ and staggering the time-centering of the fields (particle density, pressure, and magnetic) relative to the velocity, as with a leapfrog method.³³ In particular, it has been shown that stationary solutions obtained with $\alpha = \theta^2$ are more accurate than with $\alpha = \theta(\theta - 1)$.¹⁹ However, it is found here that linear eigenmodes obtained using $\alpha = \theta^2$ exhibit small-scale spatial oscillations in the absence of dissipative terms. These oscillations may significantly impact the calculated growth rate unless the features of the eigenmode are highly resolved everywhere; this is difficult to achieve in practice because the peeling-ballooning eigenmode structure is very fine (though not generally large in amplitude) on the high-field side and near the x-point of diverted plasmas, where the magnetic pitch angle is relatively shallow. In contrast, the choice $\alpha = \theta(\theta - 1)$ naturally dissipates these small-scale spatial oscillations, and growth rates obtained with this choice of α are found to be less sensitive to the spatial resolution. [The previous study which found the $\alpha = \theta^2$ choice to be favorable for steady-state calculations did not observe these small-scale oscillations, likely because it only considered axisymmetric geometry (and therefore lacked rational surfaces) and had relatively large physical dissipation.] The sensitivity of both choices of α to $\langle h^{-1} \rangle$, the average mesh element inverse length scale, is illustrated in Fig. 2. Here we define $h = \sqrt{2A}$, where A is the area of a triangular element. The inverse length scale is used in order to give more weight to the smaller elements, in which the eigenmodes are mostly localized. All of the results that follow have been obtained using $\alpha = \theta(\theta - 1)$.

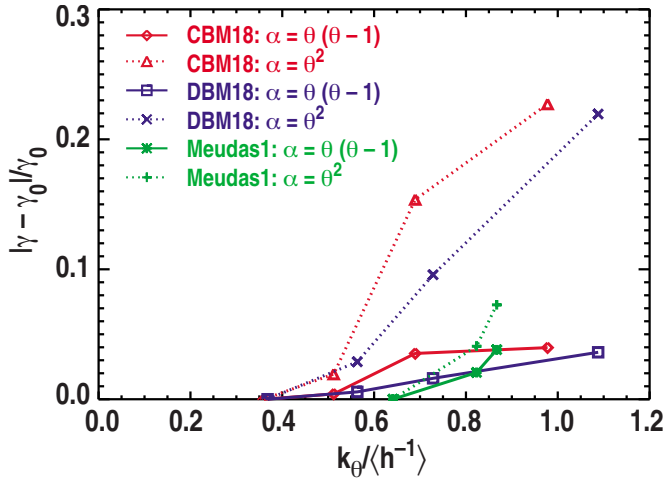


FIG. 2. (Color online) Growth rates are calculated using two different time-step methods for the three equilibria described in Sec. III A, at various mesh resolutions. Here $\langle h^{-1} \rangle$ is the average inverse element length scale of the mesh, and $k_\theta = nq_c / \langle r_c \rangle$ is the approximate poloidal wavenumber of the mode, where q_c is the safety factor at the center of the pedestal, $\langle r_c \rangle$ is the surface-averaged minor radius at the center of the pedestal, and n is the toroidal mode number ($n=10$ here). Each curve shows the fractional difference from the growth rate calculated with the most highly resolved mesh in the curve.

III. RESULTS

A. Equilibria

Benchmarks of M3D- C^1 have been carried out for three equilibria of increasing numerical difficulty, each of which is unstable to ideal peeling-ballooning modes at intermediate to high toroidal mode numbers.

- (1) The CBM18 equilibrium is a circular cross-section plasma. The pedestal width, calculated here as the full-width at half-max of the peak in $\langle \alpha \rangle$ (defined below), is approximately $\Delta\Psi \approx 0.12$. The plasma resides within a circular cross-section conformal conducting wall with a major radius of 3 m and a minor radius of 2 m. The normalized flux at the wall is $\Psi_w = 10/7$.
- (2) DBM18 differs from the CBM18 equilibrium in that it is shaped, with an ellipticity of 1.5 and triangularity of 0.2, and has a narrower pedestal than the CBM18 case, with $\Delta\Psi \approx 0.08$.
- (3) The MEUDAS1 equilibrium is designed to be characteristic of a diverted H-mode plasma in JT-60U. The calculation of linear eigenmodes of this equilibrium is significantly more challenging than for the CBM18 and DBM18 equilibria, due both to the narrower pedestal ($\Delta\Psi \approx 0.06$) and to the presence of a x-point, near which the rotational transform vanishes and the poloidal length scale of the eigenmode diverges (Fig. 3). Unlike in the CBM18 and DBM18 cases, the conducting boundary in the MEUDAS1 case is not conformal to a flux surface, and comes quite close to the foot of the pedestal.

The profiles of the surface-averaged ballooning parameter $\langle \alpha \rangle$ and normalized parallel current density $\langle |J_\parallel / B| \rangle$ are plotted for each equilibrium in Fig. 4, as a function of the normalized poloidal flux Ψ , defined as

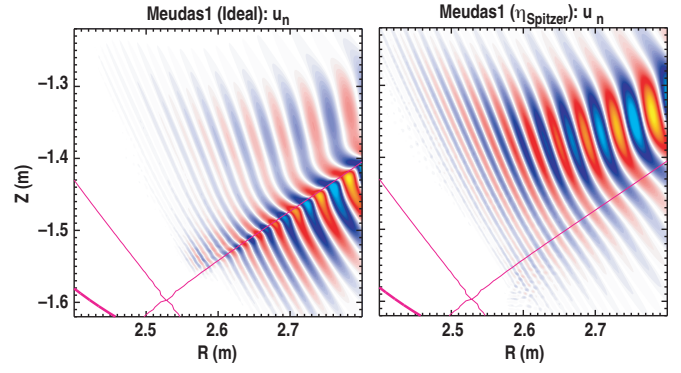


FIG. 3. (Color) The $n=10$ eigenfunction of the normal velocity for the MEUDAS1 equilibrium near the active x-point. Left: step-function plasma density and resistivity [Eqs. (10) and (11)]; right: nonuniform, continuous plasma density and Spitzer resistivity [Eqs. (14) and (15)].

$$\Psi = \frac{\psi - \psi_0}{\psi_b - \psi_0}, \quad (7)$$

where ψ is the poloidal magnetic flux per radian (to which we refer simply as the “poloidal flux”). The poloidal flux at the magnetic axis is ψ_0 , and ψ_b is the poloidal flux at the foot of the pedestal, i.e., the magnetic surface farthest from the magnetic axis for which the pressure gradient is nonzero. The surface-averaged ballooning parameter is defined to be

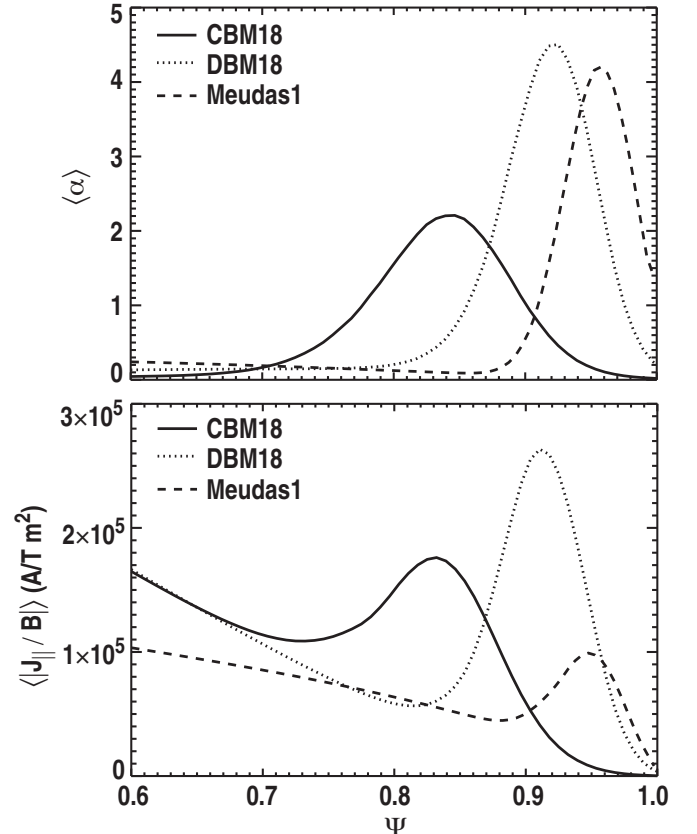


FIG. 4. The surface-averaged ballooning parameter $\langle \alpha \rangle$ and normalized parallel current density $\langle |J_\parallel / B| \rangle$ of the three equilibria studied here, as a function of the normalized poloidal flux Ψ . The geometry of each equilibrium can be seen in Fig. 7.

$$\langle \alpha \rangle = - \left(\frac{1}{2\pi^2} \right) \frac{\partial V}{\partial \psi} \sqrt{\frac{V}{2\pi^2 R_0}} \left\langle \frac{\partial p}{\partial \psi} \right\rangle, \quad (8)$$

where V is the volume enclosed by the flux surface, R_0 is the major radius at the magnetic axis, and p is the pressure. The surface average is defined as

$$\langle A \rangle = \frac{\oint_C \frac{d\ell}{B_p} A}{\oint_C \frac{d\ell}{B_p}}, \quad (9)$$

where B_p is the magnitude of the poloidal component of the magnetic field, and C is the contour defined by the poloidal projection of the magnetic surface.

B. Comparison of ideal MHD results

In ideal MHD, the plasma is modeled as a perfectly conducting fluid surrounded by a vacuum, all of which may or may not be enclosed by a perfectly conducting boundary or a resistive wall. The transition region between the plasma and vacuum is assumed to be infinitesimally thin. This assumption is difficult to model in M3D- C^1 , which makes no algorithmic distinction between the “plasma” and the “vacuum”—the outer region is simply treated as a region of high resistivity plasma—because it requires a discontinuous jump in the resistivity and mass density. A discontinuous field may be approximated simply by having a sharp but continuous transition region; the ideal result should then be obtained in the limit that the transition region narrows to zero width. However, the resolution required to obtain converged results in this limit may be extraordinarily high, even when a nonuniform mesh is used to pack resolution near the transition region. This problem is exacerbated by the use of C^1 elements, which constrain not only the fields to be continuous, but their first derivatives to be continuous everywhere (including element boundaries).

This onerous resolution requirement may be bypassed by not representing the resistivity on the C^1 finite elements at all. Specifically, the resistivity and mass density are taken to be an explicit (discontinuous) functions of the poloidal flux ψ . Thus, whenever the resistivity or density needs to be evaluated, it suffices simply to evaluate the poloidal flux at that location. The poloidal flux is typically a smooth, slowly varying quantity across the plasma-vacuum boundary, and does not require high resolution to resolve there (though high resolution is typically needed in the edge for other reasons, such as to resolve the pressure pedestal and eigenfunctions). Specifically, we choose the following profile for the resistivity:

$$\eta_{\text{ideal}}(\vec{x}) = \begin{cases} \eta_p & \text{if } \vec{x} \text{ is in the plasma region} \\ \eta_v & \text{otherwise} \end{cases} \quad (10)$$

and mass density

$$\rho_{\text{ideal}}(\vec{x}) = \begin{cases} \rho_p & \text{if } \vec{x} \text{ is in the plasma region} \\ \rho_v & \text{otherwise.} \end{cases} \quad (11)$$

The “plasma region” is defined as the simply connected region containing the magnetic axis for which the poloidal flux $\psi \in [\psi_0, \psi_i]$, where $\psi = \psi_0$ at the magnetic axis, and $\psi = \psi_i$ at the plasma-vacuum interface. (The private-flux region of a diverted plasma is not within the plasma region.) Typically $\psi_i = \psi_b$.

In practice, when carrying out numerical integrations, η and ρ can be evaluated according to Eq. (10) at each sampling point in the numerical integration quadrature (M3D- C^1 generally uses a 25-point Gaussian quadrature), and therefore η and ρ may be discontinuous even within an element domain. Thus, one need not align the elements with the plasma-vacuum boundary for this method to be effective. This technique is facilitated by M3D- C^1 's use of the flux representation of the magnetic field (axisymmetric fields are represented by $\vec{B} = \nabla\psi \times \nabla\varphi + I\nabla\varphi$, with φ the toroidal angle and $I = RB_\varphi$). Since ψ is one of the fundamental scalar fields in M3D- C^1 , value of ψ is known trivially at any point.

One potential issue with the above representation of resistivity and density is that the derivatives of η_{ideal} and ρ_{ideal} are undefined at the plasma-vacuum interface. This issue is obviated by the use of integrations-by-parts to move derivatives off of η and ρ in the weak-form equations (i.e., the weak-derivatives are used).

Recent NIMROD calculations of growth rates for the equilibria similar to the CBM18 equilibrium have found that ideal behavior is adequately recovered when $\rho_v/\rho_p \approx 10^{-2}$, $S_p \approx 10^8$ and $S_v \approx 10^3$, where S_p and S_v are the Lundquist numbers in the plasma and outer regions, respectively.¹⁵ Calculations with M3D- C^1 essentially concur with this assessment, although we find the DBM18 and MEUDAS1 equilibria to be somewhat more sensitive to the “vacuum” parameters than the CBM18 equilibrium (Fig. 5). The growth rate is seen to decrease with η_v , in accordance with the well-known argument based on energy principle considerations that treating the outer region as a resistive plasma must yield lower growth rates than using an ideal vacuum model.³⁴ Once η_v approaches the “ideal” value of approximately 10^{-8} , the growth rate becomes insensitive to further reductions in η_v ; this corresponds to the limit where the outer region is treated as an ideal plasma. (The units of η here are such that η is the inverse Lundquist number based on a one Tesla field and one meter scale-length.) The MEUDAS1 case is particularly sensitive to the outer region resistivity, with the growth rate dropping by half as the outer region transitions from a vacuum to an ideal plasma.

The ideal results presented below have been obtained with $\eta_p = 10^{-8}$ and $\eta_v = 10^{-2}$ and $\rho_v/\rho_p = 10^{-2}$, unless otherwise specified. All other explicit dissipative terms—viscosity, particle and thermal diffusivity, hyperdiffusivities, etc.—are zero.

Growth rates are calculated both using an adiabatic equation of state ($\Gamma = 5/3$) and an equation of state in which the contribution of compressional displacement is neglected ($\Gamma = 0$), where Γ is the ratio of specific heats. The “compressionless” equation of state is the preferred model in ELITE;

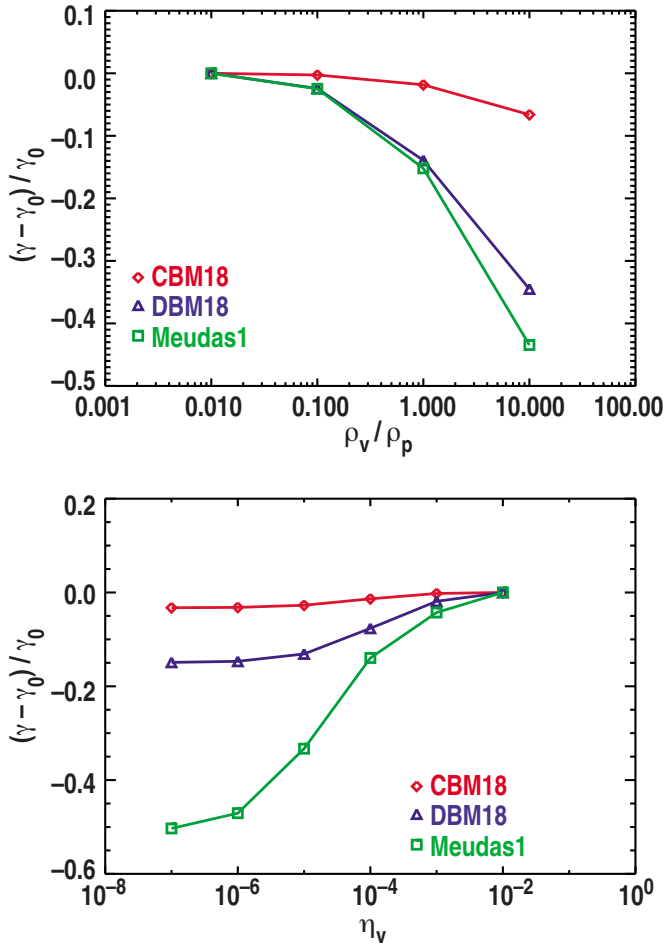


FIG. 5. (Color online) The fractional difference in the growth rate of the $n=10$ eigenmode from the case where $\rho_v/\rho_p=10^{-2}$ and $\eta_v=10^{-2}$ as ρ_v/ρ_p or η_v is varied.

the adiabatic equation of state is also implemented in ELITE, but to a lower order in the inverse mode number expansion than other terms, and is therefore expected to be less accurate at low toroidal mode numbers n .²¹

A comparison of the growth rates for each equilibrium as calculated by ELITE, GATO, and M3D-C¹ is shown in Fig. 6. The growth rates are normalized to the characteristic Alfvén frequency

$$\omega_A = \frac{B_0}{R_0 \sqrt{4\pi\rho_p}}, \quad (12)$$

where B_0 is the magnetic field strength at the magnetic axis, R_0 is the major radius of the magnetic axis, and ρ_p is the mass density at the top of the pedestal. The normal velocity ($u_n = \vec{u} \cdot \nabla \psi / |\nabla \psi|$) of the $n=10$ eigenmode for each equilibrium is shown in Figs. 7 and 8. There is generally good agreement among the different codes. The largest disagreement is found in the low- n growth rates of the MEUDAS1 case. The boundary conditions are a factor in this disagreement; ELITE assumes an infinite vacuum, whereas M3D-C¹ has a perfectly conducting wall that runs close to the plasma-vacuum interface along much of the plasma. It is expected that such a conducting wall should be stabilizing, especially to lower- n modes for which the eigenfunction tends to ex-

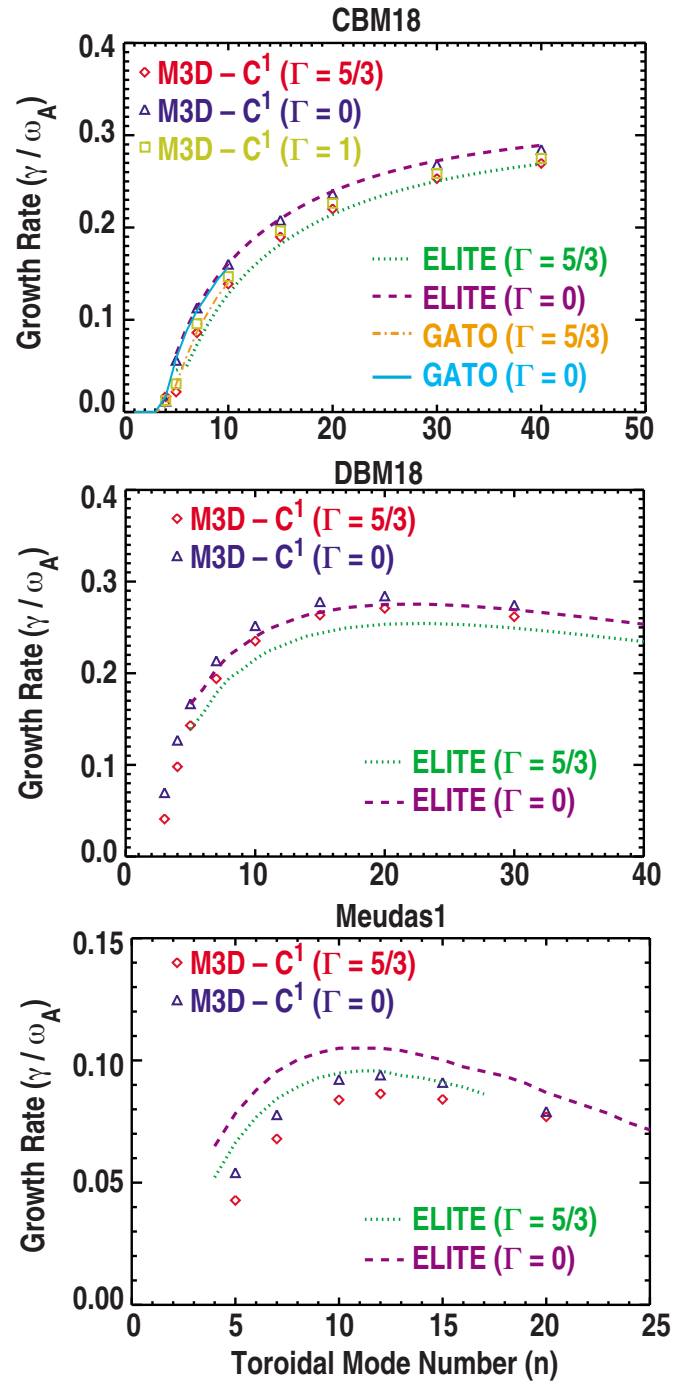


FIG. 6. (Color online) The normalized growth rate vs toroidal mode number in the ideal limit, for the CBM18, DBM18, and MEUDAS1 equilibria. Results using the isothermal equation of state ($\Gamma=1$) have also been plotted for the CBM18 case, and are bracketed by the compressionless ($\Gamma=0$) and adiabatic ($\Gamma=5/3$) results.

tend further into the outer region. However, the difference in boundary conditions is probably not enough to fully explain the growth rate discrepancy; expanding the wall outward by 8% yields only a few percent change in the growth rate of the $n=10$ eigenmode (Fig. 9). Unfortunately it is not possible to move the conducting wall more than this due to the close proximity of various poloidal field coils in the MEUDAS1 case. M3D-C¹ does not presently have the capability to model a resistive or insulating wall.

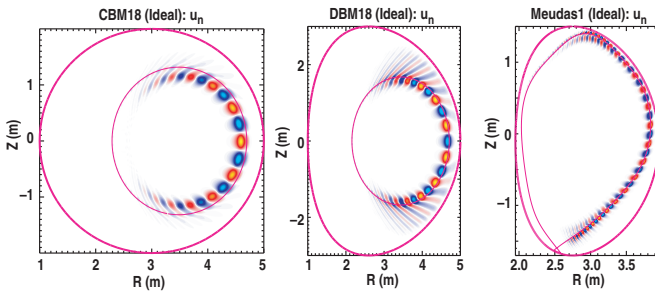


FIG. 7. (Color) The $n=10$ eigenfunction of the normal velocity for the three benchmark equilibria, as calculated by M3D-C¹. The thick curve marks the boundary of the computational domain (which is treated as a perfectly conducting wall). The thin curve represents the foot of the pedestal, which (in these cases) is the position of the vacuum-plasma interface. In the MEUDAS1 equilibrium, the foot of the pedestal coincides with the separatrix.

Another potential source of disagreement is that the position of the plasma-vacuum interface used in ELITE (and similar codes) may strongly affect the growth rate. This is discussed in more detail in the following section. For the MEUDAS1 case, the ELITE results have been computed with the plasma-vacuum interface at the 99.8% flux surface, which is converged to within a few percent. For the CBM18 and DBM18 cases, which are not diverted, this is not an issue.

The remaining disagreement between the codes in the MEUDAS1 case, as well as the smaller disagreements in the DBM18 equilibrium are too large to be accounted for by discretization errors alone. It has been shown that the growth rates are highly sensitive to the initial equilibrium, with slight differences in the method of mapping the CBM18 equilibrium (by far the easiest to resolve of the three equilibria presented here) onto the computational domain resulting in changes in the growth rate on the order of 10%.¹⁵

Finally, it should be noted that calculations of the ideal growth rate in the MEUDAS1 case have also been performed with MARG2D and ILSA. With the plasma-vacuum interface at the same position as ELITE's (in this case, at the 99.4% flux surface) MARG2D found growth rates within a few percent of ELITE, whereas ILSA produced growth rates roughly 10% lower.²⁸ ELITE and MARG2D also agree within 5% for cutoffs at 99.6% and 99.8%.

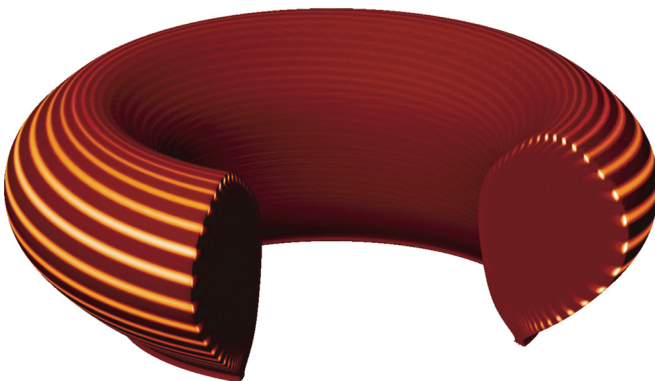


FIG. 8. (Color online) The $n=7$ eigenfunction of the normal velocity for the MEUDAS1 equilibrium. Only regions having $u_n > 0$ are highlighted. The outermost surface plotted is $\Psi=1.002$.

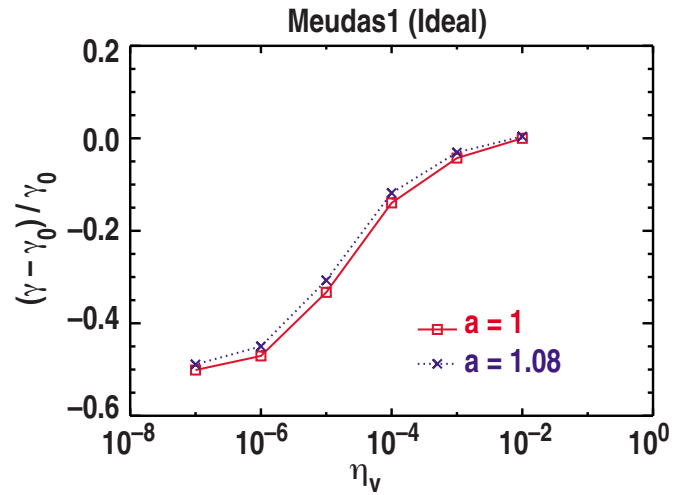


FIG. 9. (Color online) The growth rate of the $n=10$ eigenmode of the MEUDAS1 case with the conducting wall in the standard position ($a=1$) and expanded outward by 8% ($a=1.08$), vs the resistivity in the outer region η_v . At $a=1.08$, the distance of the wall from the separatrix is roughly double that at $a=1$ along the upper-half of the outboard edge.

C. The effect of moving the plasma-vacuum interface

Due to the singularity arising from the x-point of diverted magnetic geometries, many ideal MHD codes, including ELITE, typically place the plasma-vacuum interface just inside the magnetic separatrix of diverted equilibria, and thus do not include the x-point itself within the calculation of the plasma perturbed energy. For peeling-ballooning modes, the eigenfunction is not entirely localized to the closed field line region but may substantially cross the separatrix. This raises the concern that the growth rate may be sensitive to the position of the plasma-vacuum interface, and therefore it is of interest to study the limiting behavior as the plasma-vacuum interface approaches and crosses the separatrix. This issue has been addressed previously both computationally^{10,35,36} and analytically,³⁷ with the conclusion that low- n pure peeling modes, when driven by current at the cutoff, are strongly stabilized in the presence of an x-point, while the peeling-ballooning modes typically found in experimental equilibria are more modestly affected (the growth rate for a particular equilibrium can be significantly affected but the stability threshold generally only changes by a few percent). Here we quantify the sensitivity of $n=10$ peeling-ballooning mode growth rates as the plasma-vacuum interface is moved to include or exclude the separatrix.

M3D-C¹ uses cylindrical coordinates and is therefore able to include poloidal field nulls in the computational domain without difficulty. In order to assess the sensitivity of the growth rate to the position of the plasma-vacuum interface, a series of calculations have been performed with M3D-C¹ for each equilibrium, with the plasma-vacuum interface displaced from its nominal position at the foot of the pedestal. Specifically, the position of the density and resistivity transition is moved inward or outward while the pressure and magnetic field profiles are unchanged (i.e., ψ_i is changed but ψ_b is not). The distance of this displacement is measured here in terms of the offset in the normalized flux

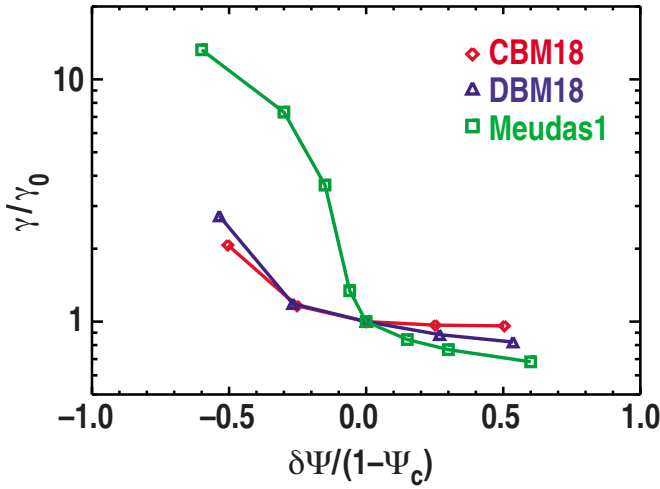


FIG. 10. (Color online) The growth rate of the $n=10$ eigenmode vs the plasma-vacuum interface offset $\delta\Psi$. Growth rates are normalized to the growth rate at zero offset; the offsets are normalized to distance from the foot of the pedestal to the center of the pedestal in the relevant equilibrium. A negative offset indicates an inward shift of the plasma-vacuum interface.

$$\delta\Psi = \frac{\psi_i - \psi_b}{\psi_b - \psi_0} \quad (13)$$

relative to the distance from the foot of the pedestal ($\Psi=1$) to the center of the pedestal ($\Psi=\Psi_c$). The center of the pedestal is defined as the magnetic surface for which $\langle\alpha\rangle$ is maximum.

The results of these calculations are shown in Fig. 10. It is evident from these results that the growth rate is sensitive to the position of the plasma-vacuum interface, particularly in the diverted equilibrium. In the MEUDAS1 case, the growth rate is increased by approximately 30% when the cutoff is moved from the separatrix to the 99.7% flux surface [corresponding to $\delta\Psi/(1-\Psi_c)=-0.06$ in this case]. Growth rates are found to be much more sensitive to inward shifts than to outward shifts.

In the results in Fig. 10, both the density transition and the resistivity transition have been moved together. Other calculations in which the density transition is held fixed while the resistivity transition is moved show that the sensitivity of the diverted case is due primarily to the position of the density profile. For example, a shift of both profiles by $\delta\Psi/(1-\Psi_c)\approx-10\%$ in the MEUDAS1 case roughly doubles the growth rate of the $n=10$ eigenmode, whereas shifting only the resistivity transition yields just a 5% increase, indicating that much of the growth rate change is due to a change in the effective inertia of the plasma.

D. The effect of realistic density and resistivity profiles

The fidelity of edge stability studies can be improved by treating both the density and resistivity profiles as continuously varying, in both the plasma and outer region. In previous ideal MHD studies of experimental discharges, realistic density profiles are generally used in the plasma region (unlike the step function density profiles used in the benchmarks above), but the density in the scrape-off-layer region (and

outside the cutoff, if a cutoff inside the separatrix is used) is approximated as zero by the vacuum model. While the density in this region is typically small, the contribution of its inertia to growth rates may still be significant.

Of course, ideal MHD codes do not include a nonuniform resistivity profile, but have instead an abrupt transition from an ideally conducting plasma to a zero conductivity vacuum region. A series of calculations have been done using M3D-C¹ to gauge the effect of including nonuniform density and resistivity profiles within the plasma. For these calculations, the mass density profile is chosen such that

$$\rho(\vec{x}) = \rho_0 p^d(\vec{x}) \quad (14)$$

with $0 < d < 1$. Thus $T_e + T_i = m_i p^{1-d} / \rho_0$, where m_i is the ion mass. Because this density profile is continuous, the density field may be (and are here) represented on the finite element basis, as opposed to the explicit functional dependence on ψ used in the previous section. While it is not necessary to do this for linear ideal calculations which are unaffected by perturbations in ρ , it is necessary for many nonideal and non-linear cases in which these perturbations must be retained. This choice does not otherwise affect the stability or convergence properties of the numerical method.

For the CBM18 case, the factor ρ_0 is chosen so that the density at the top of the pedestal is the same as in the discontinuous-density case (ρ_p), d is chosen so that the density at the foot of the pedestal is 100 times smaller than at the top of the pedestal (to facilitate comparison with the results obtained with the step-function profile), and the pressure in the outer region is such that the temperature there is roughly 41 eV. In the DBM18 case, density is treated the same way, but the edge temperature is approximately 62 eV. In the MEUDAS1 case, the density in the scrape-off layer is 20 times less than at the top of the pedestal. (The plasma-vacuum density ratio is smaller in the MEUDAS1 case in order to prevent overshoot in the finite element projection that result in negative temperatures.) Two different temperature profiles are considered with the MEUDAS1 equilibrium: one with $T_e = 38$ eV in the outer region and one with $T_e = 243$ eV. The temperature is changed by adjusting the outer region pressure while holding the density at the top and bottom of the pedestal constant. Because the pressure in the outer region is so small, the pressure gradient does not change appreciably anywhere as the temperature is changed.

One set of calculations is done in which resistivity is taken to have the same discontinuous form as used in the previous sections; in another set the resistivity is taken to have the Spitzer value, approximately

$$\eta_{\text{Spitzer}}(\vec{x}) = 2 \times 10^{-4} \sqrt{\rho_p} T_e^{-3/2}(\vec{x}) \quad (15)$$

in the same normalized units used before, with T_e in eV and ρ_p in units of $10^{13} m_i \text{ cm}^{-3}$ (the dependence on ρ_p arises from the normalization), and where we have assumed the Coulomb logarithm $\ln \Lambda \approx 17$. In all cases considered here, $T_e = T_i$. It should be noted that in all cases the Spitzer resistivity is actually lower through the core of the plasma than in the ideal case (as mentioned earlier, the growth rates are insensitive to reductions in the resistivity below roughly 10^{-8}). In the edge the Spitzer resistivity becomes somewhat

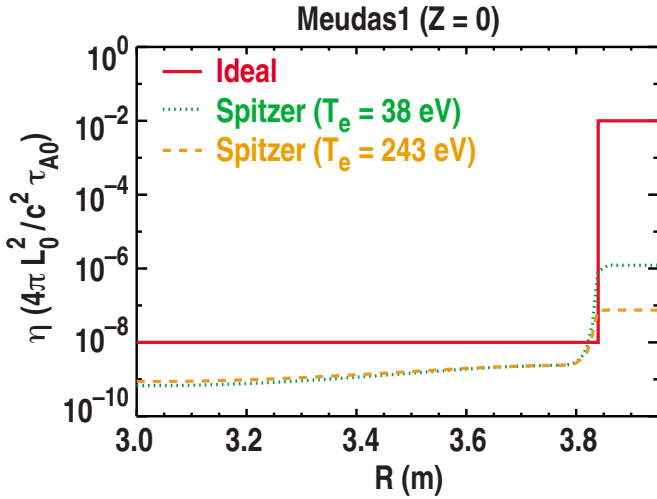


FIG. 11. (Color online) The resistivity at $Z=0$ in the MEUDAS1 equilibrium for three cases: η_{ideal} ; Spitzer resistivity with $T_e=38$ eV in the outer region; and Spitzer resistivity with $T_e=243$ eV in the outer region. The foot of the pedestal is at roughly $R=3.84$ here.

larger than in the ideal case, but in the outer region the Spitzer resistivity is far smaller than in the ideal case. The ideal resistivity profile is compared to the Spitzer resistivity for various outer region temperatures in Fig. 11.

The effect of using the continuously varying density and resistivity profiles is illustrated in Fig. 12. Replacing the uniform (within the plasma) density profile [used in the ELITE and M3D-C¹ (ideal) curves] with the nonuniform density profile results in a significant increase in the growth rate. The factor by which the growth rate increases is roughly the square-root of the factor by which the density has been reduced at the center of the pedestal. This can be understood simply by noting that occurrences of density in the ideal MHD equations may be eliminated by scaling time by the Alfvén time and velocity by the Alfvén velocity, which implies that ideal frequencies must scale as $\sim 1/\sqrt{\rho_{eff}}$, where ρ_{eff} is an effective mass density seen by the eigenmode. Equivalently, the eigenvalues of the ideal MHD operator (which does not involve density) are of the form $\rho_{eff}\omega^2$, which leads to the same conclusion. Thus, for these modes, the effect of having a continuously varying mass density in the edge is to change the effective inertia of the plasma such that ρ_{eff} is approximately the mass density at the center of the pedestal.

In the CBM18 case, using $\eta_{Spitzer}$ instead of η_{ideal} results only in a very small decrease in the growth rates of the lowest- n modes, and has practically no effect on high- n modes. In the MEUDAS1 case, however, using $\eta_{Spitzer}$ with $T_e=38$ eV in the outer region has a significant stabilizing effect at all n considered here. The observed stabilization is consistent with the results shown in Figs. 5 and 9, in which step functions for ρ_{ideal} and η_{ideal} are used, but η_v is varied. Evidently, using the Spitzer resistivity profile has an effect similar to having an instantaneous resistivity transition at the foot of the pedestal from an ideal value inside the plasma ($\eta \lesssim 10^{-8}$) to the Spitzer value in the outer region. Assuming a resistive outer region at a realistic temperature, the growth

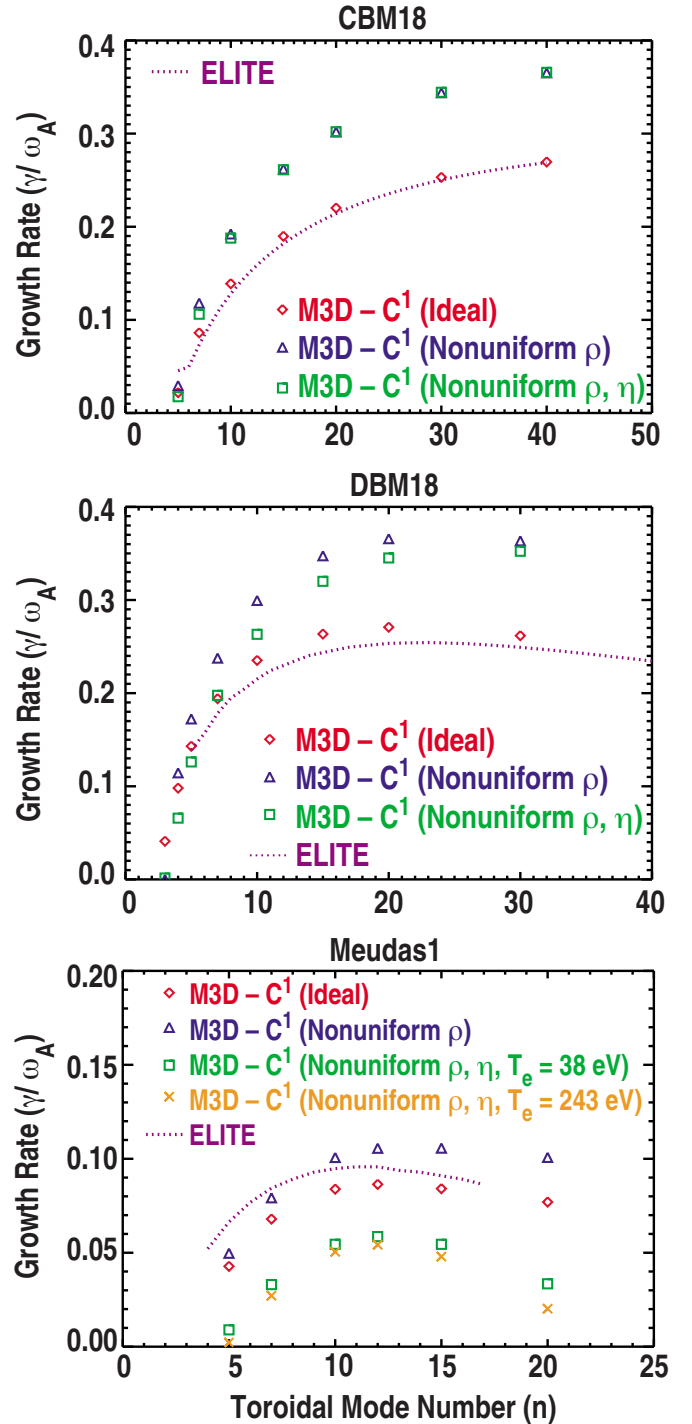


FIG. 12. (Color online) Growth rates are plotted vs toroidal mode number using η_{ideal} and ρ_{ideal} (ideal); η_{ideal} and a nonuniform ρ profile (nonuniform ρ); and $\eta_{Spitzer}$ and a nonuniform ρ profile (nonuniform ρ, η) for each equilibrium.

rates are actually closer to those obtained using an ideal plasma model of the outer region than to those obtained using an ideal vacuum model for this case.

IV. CONCLUSIONS

Growth rates of peeling-ballooning modes calculated with M3D-C¹ have been shown generally to agree well with those calculated by ideal MHD codes in the ideal limit. This

agreement should lend confidence that future nonideal peeling-ballooning calculations with M3D-C¹ may be compared meaningfully with the results of ideal codes. Boundary conditions are observed to have a small effect on calculated growth rates. The major sources of discrepancies among the codes in the ideal benchmark cases are likely the treatment of the boundary conditions, and small differences in the initial equilibria due to mapping differences.

It has been shown here that the growth rate of ideal peeling-ballooning modes in diverted equilibria is sensitive to the position of the plasma-vacuum boundary; specifically, the location of the density transition. The diverted equilibrium is in fact much more sensitive than the limited equilibria, even after accounting for the various pedestal widths of the equilibria. This may be due in part to the fact that excluding even a small region of flux-space excludes a large region of physical space near the x-point in diverted equilibria. Given this sensitivity, an ideal calculation extending only to the 99% flux surface may significantly overestimate growth rates in diverted equilibria. In the MEUDAS1 case, moving the cutoff inward from the separatrix to the 99.7% flux surface leads to a 30% increase in the growth rate, when a step function density profile is used. Of course, this sensitivity is ultimately an artifact of the strongly discontinuous density profile used for this benchmark study, and is mitigated by the use of more realistic density profiles. Studies with ELITE using experimentally relevant profiles find that the stability boundary is typically converged to within a few percent as long as the cutoff is beyond the 99.4% flux surface.¹⁰

With continuously varying density profiles, it is found that the ratio of the growth rate to the Alfvén frequency at the center of the pedestal remains roughly similar to the uniform-density case. This means that the actual growth rate will be larger than the growth rate calculated using a uniform density equal to ρ_p by roughly a factor of $\sqrt{2}$ (assuming the density at the center of the pedestal is half that at the top). This dependence of the growth rate on the density profile can be relevant, for example if a model of diamagnetic stabilization based on the ratio γ/ω_* is used to determine the stability criterion.

To varying extents for each equilibrium, lowering the resistivity in the outer region to realistic values is observed to reduce the peeling-ballooning growth rates. This general trend is expected, but has not previously been quantified. For the diverted equilibrium, this reduction is quite significant even at intermediate toroidal mode numbers ($n \sim 20$). It is found that growth rates obtained using a resistive model of the outer region more closely match those obtained using an ideal plasma model of the outer region than a vacuum model when $\eta^l \lesssim 10^{-5}$. This corresponds to an electron temperature in the outer region of roughly 10 eV, above which the ideal plasma model of the outer region is more accurate. In DIII-D, the scrape-off layer temperature in ELMing discharges is typically 50 eV.³⁸

Future work will focus on quantifying the importance of other nonideal effects on linear ELM stability, including anisotropic viscosity and thermal conductivity, gyroviscosity, and two-fluid effects.

ACKNOWLEDGMENTS

This work has also been supported in part by U.S. DOE (Contract Nos. DE-FG03-95ER54309, DE-AC05-06OR23100, and DE-AC02-09CH11466) and the support of the U.S. DOE Fusion Energy Postdoctoral Research Program. We thank X. Luo, M. Shephard, and K. Jansen of the RPI SCOREC group for the implementation and support of unstructured meshing capabilities in M3D-C¹, N. Aiba for providing the MEUDAS1 equilibrium, and S. Kruger for his contributions to the CBM18 and DBM18 equilibria. N. M. Ferraro thanks B. Burke for helpful conversations regarding NIMROD results.

- ¹G. Federici, A. Loarte, and G. Strohmayer, *Plasma Phys. Controlled Fusion* **45**, 1523 (2003).
- ²J. W. Connor, R. J. Hastie, H. R. Wilson, and R. L. Miller, *Phys. Plasmas* **5**, 2687 (1998).
- ³A. D. Turnbull, L. L. Lao, T. H. Osborne, O. Sauter, E. J. Strait, M. S. Chu, J. R. Ferron, C. M. Greenfield, A. W. Leonard, R. L. Miller, P. B. Snyder, H. R. Wilson, and H. Zohm, *Plasma Phys. Controlled Fusion* **45**, 1845 (2003).
- ⁴P. B. Snyder, H. R. Wilson, J. R. Ferron, L. L. Lao, A. W. Leonard, T. H. Osborne, A. D. Turnbull, D. Mossessian, M. Murakami, and X. Q. Xu, *Phys. Plasmas* **9**, 2037 (2002).
- ⁵G. T. A. Huysmans, *Plasma Phys. Controlled Fusion* **47**, B165 (2005).
- ⁶H. R. Wilson, S. C. Cowley, A. Kirk, and P. B. Snyder, *Plasma Phys. Controlled Fusion* **48**, A71 (2006).
- ⁷D. A. Mossessian, P. Snyder, A. Hubbard, J. W. Hughes, M. Greenwald, B. LaBombard, J. A. Snypes, S. Wolfe, and H. Wilson, *Phys. Plasmas* **10**, 1720 (2003).
- ⁸P. B. Snyder, H. R. Wilson, J. R. Ferron, L. L. Lao, A. W. Leonard, D. Mossessian, M. Murakami, T. H. Osborne, A. D. Turnbull, and X. Q. Xu, *Nucl. Fusion* **44**, 320 (2004).
- ⁹S. Saarelma, A. Alfier, M. N. A. Beurskens, R. Coelho, H. R. Koslowski, Y. Liang, I. Nunes, and JET EFDA Contributors, *Plasma Phys. Controlled Fusion* **51**, 035001 (2009).
- ¹⁰P. B. Snyder, N. Aiba, M. Beurskens, R. J. Groebner, L. D. Horton, A. E. Hubbard, J. W. Hughes, G. T. A. Huysmans, Y. Kamada, A. Kirk, C. Konz, A. W. Leonard, J. Lönroth, C. F. Maggi, R. Maingi, T. H. Osborne, N. Oyama, A. Pankin, S. Saarelma, G. Sailbene, J. L. Terry, H. Urano, and H. R. Wilson, *Nucl. Fusion* **49**, 085035 (2009).
- ¹¹K. V. Roberts and J. B. Taylor, *Phys. Rev. Lett.* **8**, 197 (1962).
- ¹²W. M. Tang, R. L. Dewar, and J. Manickam, *Nucl. Fusion* **22**, 1079 (1982).
- ¹³A. H. Glasser, C. H. Sovinec, R. A. Nebel, T. A. Gianakon, S. J. Plimpton, M. S. Chu, and D. D. Schnack, and the NIMROD Team, *Plasma Phys. Controlled Fusion* **41**, A747 (1999).
- ¹⁴D. P. Brennan, S. E. Kruger, D. D. Schnack, C. R. Sovinec, and A. Pankin, *J. Phys.: Conf. Ser.* **46**, 63 (2006).
- ¹⁵B. J. Burke, S. E. Kruger, C. C. Hegna, P. Zhu, P. B. Snyder, C. R. Sovinec, and E. C. Howell, *Phys. Plasmas* **17**, 032103 (2010).
- ¹⁶X. Q. Xu, R. H. Cohen, W. M. Nevins, G. D. Porter, M. E. Rensik, T. D. Rognlien, J. R. Myra, D. A. D'Ippolito, R. A. Moyer, P. B. Snyder, and T. N. Carlstrom, *Nucl. Fusion* **42**, 21 (2002).
- ¹⁷P. B. Snyder, H. R. Wilson, and X. Q. Xu, *Phys. Plasmas* **12**, 056115 (2005).
- ¹⁸B. D. Dudson, M. V. Umansky, X. Q. Xu, P. B. Snyder, and H. R. Wilson, *Comput. Phys. Commun.* **180**, 1467 (2009).
- ¹⁹N. M. Ferraro and S. C. Jardin, *J. Comput. Phys.* **228**, 7742 (2009).
- ²⁰H. R. Wilson, P. B. Snyder, G. T. A. Huysmans, and R. L. Miller, *Phys. Plasmas* **9**, 1277 (2002).
- ²¹P. Snyder, K. Burrell, H. Wilson, M. Chu, M. Fenstermacher, A. Leonard, R. Moyer, T. Osborne, M. Umansky, W. West, and X. Xu, *Nucl. Fusion* **47**, 961 (2007).
- ²²L. C. Bernard, F. J. Helton, and R. W. Moore, *Comput. Phys. Commun.* **24**, 377 (1981).
- ²³A. B. Mikhailovskii, G. T. A. Huysmans, W. O. K. Kerner, and S. E. Sharapov, *Plasma Phys. Rep.* **23**, 844 (1997).
- ²⁴A. H. Glasser, Los Alamos Technical Report No. LA-UR-95-528, 1995.

- ²⁵E. Strumberger, S. Günter, P. Merkel, S. Riondato, E. Schwarz, C. Tichmann, and H. P. Zehrfeld, *Nucl. Fusion* **45**, 1156 (2005).
- ²⁶S. Tokuda and T. Watanabe, *Phys. Plasmas* **6**, 3012 (1999).
- ²⁷N. Aiba, S. Tokuda, M. Furukawa, N. Oyama, and T. Ozeki, *Nucl. Fusion* **49**, 065015 (2009).
- ²⁸C. Konz, P. B. Snyder, N. Aiba, L. D. Horton, C. F. Maggi, S. Günter, and P. J. McCarthy, the ASDEX Upgrade, and DIII-D Teams, Proceedings of the 35th EPS Conference on Plasma Physics, Hersonisso, Greece, 2008, Vol. 32D, p. 2.071.
- ²⁹D. H. Liu and A. Bondeson, *Comput. Phys. Commun.* **116**, 55 (1999).
- ³⁰S. I. Braginskii, in *Reviews of Plasma Physics*, edited by M. A. Leontovich (Consultants Bureau, New York, 1965), Vol. 1, pp. 205–311.
- ³¹S. C. Jardin, *J. Comput. Phys.* **200**, 133 (2004).
- ³²J. Breslau, N. Ferraro, and S. Jardin, *Phys. Plasmas* **16**, 092503 (2009).
- ³³E. J. Caramana, *J. Comput. Phys.* **96**, 484 (1991).
- ³⁴J. P. Freidberg, *Rev. Mod. Phys.* **54**, 801 (1982).
- ³⁵G. T. A. Huysmans, *Plasma Phys. Controlled Fusion* **47**, 2107 (2005).
- ³⁶S. Y. Medvedev, A. A. Martynov, Y. R. Martin, O. Sauter, and L. Villard, *Plasma Phys. Controlled Fusion* **48**, 927 (2006).
- ³⁷A. J. Webster and C. G. Gimblett, *Phys. Rev. Lett.* **102**, 035003 (2009).
- ³⁸J. A. Boedo, D. L. Rudakov, E. Hollmann, D. S. Gray, K. H. Burrell, R. A. Moyer, R. Fonck, P. C. Stangeby, T. E. Evans, P. B. Snyder, A. W. Leonard, M. A. Mahdavi, M. J. Schaffer, W. P. West, M. E. Fenstermacher, M. Groth, S. L. Allen, C. J. Lasnier, G. D. Porter, N. S. Wolf, R. J. Colchin, L. Zeng, G. Wang, J. G. Watkins, T. Takehashi, and the DIII-D Team, *Phys. Plasmas* **12**, 072516 (2005).